Role of composition, bond covalency, and short-range order in the disordering of stannate pyrochlores by swift heavy ion irradiation

Cameron L. Tracy, Jacob Shamblin, Sulgiye Park, Fuxiang Zhang, Christina Trautmann, Maik Lang, and Rodney C. Ewing

Phys. Rev. B **94**, 064102 — Published 3 August 2016

DOI: 10.1103/PhysRevB.94.064102

Role of composition, bond covalency, and short-range order in the disordering of stannate pyrochlores by swift heavy ion irradiation

Cameron L. Tracy[1], Jacob Shamblin[2], Sulgiye Park[1], Fuxiang Zhang[3], Christina Trautmann[4,5], Maik Lang[2], Rodney C. Ewing[1]

[1] *Department of Geological Sciences, Stanford University, Stanford, CA 94305, USA*

[2] *Department of Nuclear Engineering, University of Tennessee, Knoxville, TN 37996, USA*

[3] *Materials Science and Technology Division, Oak Ridge National Laboratory, Oak Ridge, TN 37831, USA*

[4] *GSI Helmholtzzentrum für Schwerionenforschung, 64291 Darmstadt, Germany*

[5] *Technische Universität Darmstadt, 64287 Darmstadt, Germany*

ABSTRACT

$A_2Sn_2O_7$ (A = Nd, Sm, Gd, Er, Yb, and Y) materials with the pyrochlore structure were irradiated with 2.2 GeV Au ions to systematically investigate disordering of this system in response to dense electronic excitation. Structural modifications were characterized, over multiple length scales, by transmission electron microscopy, x-ray diffraction, and Raman spectroscopy. Transformations to amorphous and disordered phases were observed, with disordering dominating the structural response of materials with small A-site cation ionic radii. Both the disordered and amorphous phases were found to possess weberite-type local ordering, differing only in that the disordered phase exhibits a long-range, modulated arrangement of weberite-type structural units into an average defect-fluorite structure, while the amorphous phase remains fully aperiodic. Comparison with the behavior of titanate and zirconate pyrochlores showed minimal influence of the high covalency of the Sn-O bond on this phase behavior. An analytical model of damage accumulation was developed to account for simultaneous amorphization and recrystallization of the disordered phase during irradiation.

I. INTRODUCTION

Ternary oxides with the composition $A_2B_2O_7$ and the pyrochlore structure exhibit unique physical behaviors due to their geometric frustration, with spin liquid states, spin ice states, metal-insulator transitions, and superconductivity having been reported[1,2]. They find potential application as matrices for the dilution and immobilization of nuclear waste[3], thermal barrier coatings for gas turbine engines[4,5], and electrolytes for solid oxide fuel cells[6]. The pyrochlore structure is observed for $A_2B_2O_7$ compounds in which the A-site is occupied by a large cation (such as a trivalent lanthanide, actinide, or Y) and the B-site by a smaller cation (typically a

tetravalent transition metal or group 14 element)[7]. Its stability is constrained by the ratio of the ionic radii of the *A*- and *B*-site cations (r_A and r_B, respectively), such that the pyrochlore structure generally forms when $1.46 \lesssim r_A/r_B \lesssim 1.78$. A defect-rich, fluorite-like structure usually forms when r_A/r_B is below this stability range and structures of lower symmetry form above[8,9].

In the pyrochlore structure (space group $Fd\bar{3}m$), *A*-site cations adopt eightfold scalenohedral coordination with anions, while *B*-site cations adopt sixfold distorted octahedral coordination[7]. Mixed corner- and edge-sharing of the polyhedra yields a cubic unit cell. The pyrochlore structure can be considered an anion-deficient derivative of the fluorite structure (space group $Fm\bar{3}m$), which is exhibited by AO_2 compounds and consists of a face-centered cubic array of cations with anions occupying the tetrahedral interstices. These two structures differ in that the pyrochlore structure features ordering of two aliovalent cations on the fluorite-like cation sublattice, while one-eighth of the tetrahedral interstices are vacant and some anions are slightly displaced from the ideal tetrahedral sites. Under high-temperature[6,10] or high-pressure[11,12] conditions, many pyrochlore compounds undergo an order-disorder phase transformation wherein the pyrochlore superstructure ordering is lost, leaving only fluorite-like long-range ordering. This is driven by mixing of cations onto a single crystallographic site and the formation of anti-Frenkel pairs, such that the resulting disordered structure is often described as "defect-fluorite."

Alternatively, under temperature and pressure conditions for which the ordered pyrochlore phase is stable, disordering can be induced by dense electronic excitation, such as that resulting from irradiation of a material with high-energy heavy ions[13–18]. Ions in this high-velocity regime (having specific energies greater than ~1 MeV/u) interact with materials primarily through the deposition of energy to electrons, rather than the elastic nuclear collisions

that dominate at low ion velocities. This produces a state of warm dense matter, lasting on the order of 100 fs, during which a hot electron-hole plasma coexists with a relatively low-temperature, ionized atomic subsystem[19,20]. The excitation of electrons to antibonding orbitals in the conduction band makes accessible phase transformation pathways precluded under equilibrium conditions, while subsequent electron-hole recombination yields phonon emission and local heating, driving the material further from equilibrium[21]. These processes occur within a nanometric region along the roughly linear paths of swift heavy ions in solids. Following relaxation of the ion-solid interaction region, each ion leaves a cylindrical track, typically several nanometers in diameter, within which the irradiated material is structurally and chemically modified.

Patel *et al.*[14], Lang *et al.*[15,16,22,23], and Sattonnay *et al.*[17,18,24] have shown experimentally that the specific phase transformations induced by swift heavy ion irradiation of pyrochlore compounds depend strongly on their composition. Molecular dynamics simulations support their findings[13]. Compounds with similar cation ionic radii (small r_A/r_B) favor an order-disorder transformation to the defect-fluorite phase, while those with a large cation size mismatch (large r_A/r_B) instead transform to an amorphous phase. For intermediate r_A/r_B, a complex ion track morphology is observed wherein an annular track shell of disordered, crystalline material surrounds an amorphous cylindrical track core[16,22]. This composition-dependence of the response of pyrochlore materials to dense electronic excitation is most often attributed to the influence of the cation size mismatch on the energetics of cation site exchange and the stability of the defect-fluorite phase, as demonstrated by atomistic simulations[25,26].

Bond covalency has been proposed as another predictor of radiation tolerance, defined as the ability of a material to resist amorphization under irradiation. Naguib and Kelly[27], and more

recently Trachenko *et al.*[28–30], argue that covalently-bonded materials are amenable to the formation of amorphous polyhedral networks because the energy landscapes that govern their atomic structures are based on short-range covalent forces. In contrast, longer-range forces associated with ionic bonding produce energetics unfavorable for the formation of these amorphous structures, and thus promote recrystallization following dense atomic displacement. In this way, the superior glass-forming ability of covalently-bonded materials yields resistance to irradiation-induced amorphization inferior to that of more ionically-bonded materials. This bond type criterion for radiation tolerance has been proposed as an alternative explanation for the observed compositional trends in the amorphization and disordering of pyrochlore materials by swift heavy ion irradiation[28,29].

While the response of pyrochlores to irradiation in the electronic stopping regime has been extensively investigated, much of this work was restricted to a narrow composition range; the majority of studies have focused exclusively on titanate and zirconate compounds (*B* = Ti, Zr)[13–18,23,24,31]. The titanates are prone to amorphization, while the zirconates tend to disorder, retaining their crystallinity. This is consistent with both cation ionic radius and bond covalency criteria for amorphization resistance, as Ti^{4+} is smaller than Zr^{4+} (yielding an r_A/r_B closer to the upper stability limit)[32] and forms a more covalent bond with O^{2-} [33,34]. Thus, the study of these systems is insufficient to distinguish the effects and relative influence of the cation size mismatch and the bond covalency on the phase behavior of pyrochlores and related complex oxides under extreme conditions. In this respect, study of a *B*-site cation substitution that decreases r_A/r_B while increasing *B*-O bond covalency, or *vice versa*, is advantageous. The stannate pyrochlores (*B* = Sn) are interesting in this respect, as density functional theory (DFT) calculations[33,35,36] and experimental characterization of the electron density distribution[37] show

relatively high covalency of their Sn-O bonds (higher than that of the Ti-O bond), while the ionic radius of Sn is intermediate to those of Ti and Zr[32]. Thus, a radiation response governed by the ionic radii of the *A*- and *B*-site cations would yield mixed amorphization and disordering of the stannate pyrochlores, a response between those of the titanates and zirconates. In contrast, bond covalency-dependence of the phase response would result in high susceptibility to amorphization, and radiation tolerance inferior to that of the titanate system.

We report an investigation of the structural response of stannate pyrochlores with *A*-site cations spanning the lanthanide series, along with Y, to irradiation with 2.2 GeV Au ions. Simultaneous amorphization and disordering was observed and analytically modelled. The relative extent of each transformation varies monotonically with the *A*-site cation ionic radius. The tendency of stannate pyrochlores to disorder, rather than amorphize, is shown to be intermediate to those of titanate and zirconate pyrochlores, a result inconsistent with a substantial influence of bond covalency on the radiation response. The local structures of amorphized and disordered compounds are shown to be similar, with all compositions studied exhibiting short-range weberite-type ordering[38] that, in the disordered phase, is modulated to yield an average, long-range defect-fluorite structure.

II. EXPERIMENTAL METHODS

Powders of $A_2Sn_2O_7$ (A = Nd, Sm, Gd, Er, Yb, and Y) were synthesized by solid-state methods. Stoichiometric ratios of A_2O_3 and SnO_2 powders were mixed and calcined at 1400 °C for 24 hours. X-ray diffraction measurements confirmed a pyrochlore structure. The powders were uniaxially compressed with a pressure of 25 MPa, producing 40 μm thick wafers with typical densities of 60% theoretical density and typical grain sizes of several micrometers. This

sample form is based on that used in previous swift heavy ion irradiation experiments[39]. The low sample density allows for the use of relatively thick samples, facilitating their handling, while still minimizing the amount of material through which ions pass, and thus the variation in ion energy deposition as a function of sample penetration depth. Additionally, the presence of empty space between dense grains in the compacted powder allows the samples to accommodate any potential irradiation-induced swelling without experiencing significant stresses or the loss of sample integrity. While the presence of more material/atmosphere interfaces in these compacted powders, compared to a dense pellet, may enhance some surface phenomena, these effects are expected to be small, considering that the micrometric scale of the polycrystal grains is several orders of magnitude larger than the nanometric scale of the ion tracks.

The wafers were irradiated using beamline X0 of the UNILAC accelerator at the GSI Helmholtz Centre for Heavy Ion Research in Darmstadt, Germany. All samples were simultaneously exposed to a beam of 2.2 GeV Au ions, oriented such that the beam direction was perpendicular to the wafer faces. The ion flux was maintained below 2×10^{9} ions cm^{-2} s^{-1} to prevent bulk heating of the samples. Irradiation was carried out to ion fluences ranging from 1×10^{11} to 3×10^{13} ions cm^{-2}, with typical fluence uncertainties of 10%. The penetration of ions into the samples was calculated using the SRIM code[40], correcting for the low densities of the pressed powders. All ions were found to pass completely through the samples, depositing a nearly constant energy per unit path length to the material's electrons. The nuclear energy loss was, across the entire sample thickness, more than three orders of magnitude less than the electronic energy loss, such that the effects of electronic excitation were isolated.

The shapes of the nanometric ion tracks were determined through direct imaging by transmission electron microscopy (TEM). Small portions of wafers of each material, irradiated to

a fluence of 1×10^{11} ions cm^{-2}, were crushed into a powder. At this low ion fluence tracks were well-separated, allowing individual tracks to be easily distinguished. The powders were dispersed onto holey carbon-coated copper TEM grids and imaged using a JEOL 2010F microscope operating at 200 kV in bright-field mode.

Irradiation-induced modifications to the long-range atomic structures of these materials were characterized by angle-dispersive synchrotron x-ray diffraction (XRD), performed at beamline B2 of the Cornell High Energy Synchrotron Source (CHESS). All samples were exposed in transmission geometry to a 1 mm^2 monoenergetic beam with a wavelength of λ = 0.496 Å. Debye rings were recorded on a Mar charge-coupled device (CCD) detector for 300 s. The detector images were integrated in the azimuthal direction using the software Fit2D[41]. Phase fractions of the irradiation-induced amorphous phase, if present, were determined by the peak deconvolution technique of Lang *et al.*[15]. Total pattern fitting was performed using pseudo-Voigt functions to fit both sharp diffraction maxima and diffuse scattering bands arising from the amorphous phase, while a sixth-order polynomial was fit to the background. In this way, the contributions to each pattern from the amorphous and crystalline fractions were distinguished. Qualitative measures of the amorphous fractions were obtained by calculating the ratio of the sum of integrated intensities, or peak areas, of diffuse scattering bands to the summed integrated intensities of all peaks. This analysis provides only qualitative data, since the relation between phase fraction and the integrated intensity of the XRD signal from an individual phase is complex. However, this method is suitable for the comparison of relative amorphous fractions in structurally- and compositionally-similar materials, among which this relation will not vary greatly.

Irradiation-induced modifications of the local atomic arrangements in these materials were studied by Raman spectroscopy. Spectra were recorded in backscattering geometry with a Horiba Jobin Yvon LabRAM HR800 micro-Raman spectrometer with a 20 mW HeNe laser excitation source (λ = 632.8 nm). A diffraction grating with 1800 grooves/nm provided a spectral resolution of approximately 0.01 nm. Each sample was exposed to a beam spot of ~2 μm in diameter. All measurements were performed for 40 s, and three measurements were averaged to obtain final spectra for each sample.

III. RESULTS AND DISCUSSION

A. Transmission electron microscopy: ion track shape

TEM imaging of the irradiated samples revealed the presence of parallel, continuous ion tracks in all materials. Fig. 1 shows a representative micrograph of tracks in $Nd_2Sn_2O_7$. Contrast between the in-track regions and the surrounding, unirradiated matrix indicates structural modification of the material within the tracks. No significant change in track diameter as a function of sample depth was observed. This is consistent with the nearly constant electronic energy loss of the Au ions throughout the entire sample thickness, as shown by the results of SRIM calculations in Fig. 2. The variation in electronic energy loss as a function of sample penetration depth was, for all compounds, less than 2.3 keV/nm. These results indicate that the ion tracks can be accurately modelled as cylindrical objects of constant diameter, containing material that has been transformed from the initial pyrochlore structure.

Precise determination of the track diameters is hindered by the indistinct interface between the modified and unmodified regions. This is likely due to the significant internal track phase heterogeneity that is common to pyrochlore compounds[13,16,18]. Typically, an amorphous

track core is surrounded by a disordered or defect-rich track shell. Each region will yield different contrast in TEM imaging, resulting in the observed smearing of contrast at the parallel track edges. Due to uncertainty in the precise location of the track boundaries, the track diameter as a function of composition was not quantified using TEM. However, the variance in track size among the materials studied is small, with all showing track diameters of roughly 6 nm.

B. X-ray diffraction: long-range structure

Representative XRD patterns from several of the compounds studied, both unirradiated and irradiated to various ion fluences, are shown in Fig. 3. Patterns collected from the unirradiated samples correspond to a well-crystallized pyrochlore phase. The most intense diffraction maxima (for example, the (222), (004), (044), and (226) peaks) arise from fluorite-like substructure ordering, while the less-intense maxima (for example, the (111), (133), and (155) peaks) are indicative of the pyrochlore superstructure.

The XRD patterns collected from all materials evolve with increasing ion fluence, indicating the loss of the initial pyrochlore structure due to electronic excitation-induced phase transformations. Three changes to the patterns are observed: broadening of the initial diffraction maxima, attenuation of some or all of the initial maxima, and growth of broad diffuse scattering bands. Peak broadening can result from either the accumulation of heterogeneous microstrain around defects formed by atomic displacement or the reduction of crystallite sizes due to grain fragmentation[42]. Attenuation of the initial diffraction maxima indicates the loss of ordering characteristic of the pyrochlore structure. An order-disorder transformation to the defect-fluorite phase yields attenuation of only the maxima corresponding to the pyrochlore superstructure, while those arising from the fluorite-like ordering remain[6]. In contrast, the formation of an amorphous phase within the ion tracks causes the attenuation of all initial maxima as the

material's crystalline fraction decreases with increasing ion fluence. The growth of broad scattering bands in the approximate angular ranges 2θ = 6-11, 13-8, and 18-20° provides further evidence of amorphization, as this signal is typical of diffuse scattering from an aperiodic atomic arrangement[43].

The nature of the transformations induced in stannate pyrochlores by electronic excitation shows clear dependence on composition. Amorphization is evident in all materials, while several also exhibit simultaneous disordering. The extent to which amorphization, rather than disordering, dominates the radiation response of a particular compound is proportional to the ionic radius of the *A*-site cation. The lanthanide elements are chemically similar, yet their ionic radii decrease across the lanthanide series, while the ionic radius of Y is intermediate to those of Gd and Er. Thus, at the highest ion fluence achieved, 3×10^{13} ions cm^{-2}, $Nd_2Sn_2O_7$, $Sm_2Sn_2O_7$, and $Gd_2Sn_2O_7$ are fully transformed to an amorphous phase. In contrast, the pyrochlores with smaller *A*-site cations retain a significant amount of crystallinity at this fluence, although all compounds completely lose pyrochlore superstructure ordering by 1.5×10^{13} ions cm^{-2}. $Yb_2Sn_2O_7$, which has the smallest *A*-site cation among the materials studied, and is the most resistant to amorphization, consists mainly of the defect-fluorite phase at the highest ion fluence achieved. Because the electronic energy deposition per unit ion path length in these materials increases with decreasing r_A, due to increasing density (with the exception of $Y_2Sn_2O_7$, see Fig. 2), this compositional trend cannot be attributed to variation in energy deposition and must therefore result from ionic radius effects. The observed mixed phase behavior of the stannate pyrochlores, ranging from complete amorphization to predominant disordering, is intermediate to that of the titanate and zirconate pyrochlores. These pyrochlore systems show similar trends in radiation response with *A*-site cation substitution, yet amorphization dominates in all titanate pyrochlores,

while most zirconates only disorder under swift heavy ion irradiation. Under identical irradiation conditions, titanates with the same *A*-site cations show substantially higher amorphous fractions than the stannates[31]. In contrast, only a few zirconate pyrochlores with large r_A/r_B have been observed to amorphize in response to irradiation, and the extent of amorphization is typically small relative to that of disordering[18,44].

Irradiation of stannate pyrochlores with ions of low specific energies, for which elastic nuclear collisions dominate the energy deposition, show compositional trends in disordering and amorphization similar to those reported here for swift heavy ion irradiation[45]. In both cases, compounds with large *A*-site cations tend to amorphize, while those with smaller *A*-site cations preferentially disorder to a long-range defect-fluorite structure. Similar correspondence has been observed between the effects on the structures of titanate and zirconate pyrochlores of irradiation in the nuclear[46] and electronic energy loss[15,16,22] regimes. This suggests that the observed phase behavior is intrinsic to the materials, based on the energetics of their recovery from a perturbed state and the effects of the cation size mismatch on these energetics. These phase processes are thus a general feature of the order-disorder dynamics of these systems, rather than a response specific to a certain mechanism of energy deposition and atomic displacement, such as a nuclear collision cascade or dense ionization.

Amorphous phase fraction data obtained from XRD measurements, shown in Fig. 4, further illustrate the composition-dependence of the electronic excitation-induced pyrochlore-to-amorphous transformation. The amorphous fraction, f_A, of an irradiated material at a given ion fluence decreases with decreasing *A*-site cation ionic radius. In all materials, the initial linear accumulation of the amorphous phase gives way to saturation at higher ion fluences. For the compounds resistant to amorphization, this saturation occurs at amorphous fractions below unity,

indicating that a steady state is achieved wherein further irradiation yields amorphization and recrystallization of initially amorphous material in equal parts. Saturation of the amorphous fraction below unity is uncommon, but has been previously observed in $Lu_2Ti_2O_7$, the titanate pyrochlore with the smallest r_A/r_B, irradiated with ions of low specific energy[47].

Because ion tracks in these stannate pyrochlores are continuous cylinders of nearly constant diameter as a function of sample penetration depth, fitting of a simple, two-dimensional statistical rate model to phase fraction data yields quantitative information about ion track dimensions and morphologies. Typically, Poisson expressions are used for this purpose. Assuming no variation of the tracks with penetration depth, the only parameters needed to model damage accumulation as a function of ion fluence are the cross-sectional areas, σ, for which each induced phase modification occurs following a single ion impact. The form of the model depends on the manner in which the overlap of these cross-sectional influence regions yields further phase modification. A single-impact model, first developed by Gibbons[48], is most often used[16,17,23,24,49]. This model assumes that complete modification of the in-track material is achieved in a single ion impact and that further impacts to this region (track overlap) yield no additional modification. The modified phase fraction, f_M, is expressed as:

$$f_M(\Phi) = A(1 - e^{-\sigma\Phi}) \quad (1)$$

where Φ is the ion fluence, A is a dimensionless fitting parameter, and σ is the cross-sectional area in which the irradiated material is modified following a single ion impact.

The single-impact model predicts an initial linear increase in modified phase fraction with ion fluence, followed by saturation as the probability of track overlap increases. This behavior is consistent with the buildup of the amorphous fraction shown in Fig. 4. However, this model accounts for the production of only a single phase during irradiation, rather than the

simultaneous formation of amorphous and disordered phases observed here. Furthermore, saturation of the modified phase fraction at a value below unity, as shown in Fig. 4 for the amorphization-resistant stannate pyrochlores, is modelled only by the fitting parameter A in Eq. (1), which has no physical meaning. This is because the model does not account for recrystallization of initially amorphous material caused by ion energy deposition. The observation of disordered shells around the peripheries of ion tracks in many pyrochlores indicates that recrystallization plays an important role in damage accumulation[13,16,18], and TEM studies of ion tracks in fluorite-structured CeO_2 have demonstrated the recovery of initially damaged material through recrystallization of track shells[50]. A more complex model of damage accumulation in pyrochlore materials was proposed by Sattonnay *et al.*[18], which considers the incremental buildup of damage in track peripheries through a multiple-impact mechanism. While this model does account for the formation of multiple new phases during irradiation, it does not physically describe the saturation of f_A below unity, as observed here, and does not account for the recrystallization of previously damaged volume.

To represent the multiple, simultaneous phase transformations in the stannate pyrochlores as a function of ion fluence, a model accounting for both damage accumulation and recrystallization (partial recovery of the initial damage) was developed. This model assumes a track evolution process wherein the energy deposited to a material by a swift heavy ion initially causes the loss of long-range order in the core of the ion-solid interaction region, followed by recrystallization of the track periphery prior to dissipation of the deposited energy to the surrounding matrix and quenching of the track structure. This process has been observed in molecular dynamics simulations[13] and is supported by analytical calculations using an inelastic thermal spike model[22]. It yields a final ion track in which an amorphous core of cross-sectional

area σ_A is surrounded by a disordered shell of area σ_D. Because TEM observation of heterogeneous ion tracks in pyrochlores commonly reveals the presence of the disordered phase only at the interface between the track and the surrounding undamaged matrix, it is assumed that recrystallization occurs epitaxially, with the pyrochlore matrix acting as a template for the kinetically-favorable formation of the disordered defect-fluorite phase. Competition between amorphization and epitaxial recrystallization gives rise to the observed saturation of f_A at values below unity for those stannate pyrochlore compounds in which disordering is the primary structural modification. Following the analysis of Morehead and Crowder[51], this phase modification mechanism yields the expressions:

$$\frac{df_A}{dt} = \sigma_A \varphi (1 - f_A) - \sigma_D \varphi f_A (1 - f_A) \tag{2}$$

$$\frac{df_D}{dt} = \sigma_D \varphi f_A (1 - f_A) + \sigma_D \varphi f_P - \sigma_A \varphi f_D \tag{3}$$

$$\frac{df_P}{dt} = 1 - \sigma_D \varphi (1 - f_P) - \sigma_A \varphi (1 - f_P) \tag{4}$$

where f_A, f_D, and f_P, are the amorphous, disordered, and pyrochlore fractions, respectively; σ_D and σ_A are the cross-sectional areas for the formation of the latter two phases; and φ is the ion flux. Ion-solid interaction causes an amount of material proportional to σ_A to transform to the amorphous phase, and an amount of material proportional to σ_D to transform to the disordered phase. The probability of an initially crystalline region becoming amorphous is proportional to the crystalline fraction of the material, $(1-f_A)$, while the probability of an ion impact disordering a region with the ordered pyrochlore structure is proportional to f_P. Because the epitaxial recrystallization of the disordered phase from initially amorphous material requires the presence of a crystalline/amorphous interface, the probability of this process is taken to be $f_A(1-f_A)$, as this term scales with the amount of this interface present in the material[52].

Solving this system of equations [Eqs. (2)-(4)] yields analytical expressions for the amorphous and disordered phase fractions as a function of ion fluence:

$$f_A(\Phi) = \frac{1 - e^{-\sigma_A \Phi + \sigma_D \Phi}}{1 - \left(\frac{\sigma_D}{\sigma_A}\right) e^{-\sigma_A \Phi + \sigma_D \Phi}} \tag{5}$$

$$f_D(\Phi) = \frac{(\sigma_A - \sigma_D) e^{\sigma_D \Phi}}{\sigma_A e^{\sigma_A \Phi} - \sigma_D e^{\sigma_D \Phi}} - e^{\Phi(\sigma_D - \sigma_A)} \tag{6}$$

Eq. (5) predicts eventual saturation of the amorphous fraction at $f_A = 1$ when $\sigma_A \geq \sigma_D$, and saturation at at $f_A = \sigma_A/\sigma_D$ otherwise. For $\sigma_D = 0$, Eq. (5) is identical to the single impact model, Eq (1), with the exception that it does not feature a dimensionless parameter A governing the saturation value of the transformed phase fraction.

Eq (5) was fit to the experimental amorphous phase fraction values in Fig. 4, showing good agreement with the data and yielding track areas for amorphization and disordering transformations, show in Fig. 5. The total track cross-sectional area ($\sigma_A+\sigma_D$) is relatively constant with A-site cation substitution, at ~14 nm^2. This means that all stannate pyrochlores will lose their initial pyrochlore structures at a similar rate, as a function of fluence, although the phases formed within the tracks and their fractions vary with composition. For example, as shown in Fig. 4, at a fluence of 1.7×10^{13} ions cm^{-2} about 90% of a material will have been modified by ion impact to produce either an amorphous or a disordered phase. The lack of variation in total ion track dimensions with composition is consistent with the TEM observations discussed previously, although the track diameter predicted from these XRD results, ~4.2 nm, is smaller than the ~6 nm diameter determined from TEM. A similar discrepancy between track dimensions determined from XRD and TEM characterization was observed in a prior study of titanate and zirconate pyrochlores[16]. In this earlier work, track diameters determined from XRD

measurements were consistently ~2 nm smaller than those determined form TEM imaging, a discrepancy which agrees very well with that reported here. This effect may be related to differences in the segments of the ion tracks that are probed by XRD and TEM techniques. XRD is sensitive only to changes in the long-range structure of a material, while TEM contrast can result from a high point defect concentration in a region that otherwise retains its structure[16]. Thus, a possible explanation of the observed track size discrepancy is the presence of a ~1 nm thick, pyrochlore-structured, point defect-rich shell around the ion tracks, which yields an additional 1 nm thick region of TEM contrast without significantly influencing the XRD determination of track dimensions.

A monotonic trend of increasing amorphous fraction within individual ion tracks with increasing r_A/r_B is evident. σ_A and σ_D vary regularly as a function of r_A/r_B, except for a slight deviation for $Y_2Sn_2O_7$ ($r_A/r_B = 1.477$). This is likely due to the low mass of Y relative to the lanthanides, resulting in a lower density of this material and hence a lower ion electronic energy loss per unit path length (shown in Fig. 2). Similar deviation for this compound has been observed in the response of titanate pyrochlores to the same irradiation conditions[31] and the response of stannate pyrochlores to irradiation with ions of low specific energy[45].

The two compounds with the largest *A*-site cations, $Nd_2Sn_2O_7$ and $Sm_2Sn_2O_7$, exhibit fully amorphous tracks ($\sigma_D = 0$), while those with relatively small *A*-site cations exhibit predominantly disordered, crystalline tracks ($\sigma_D > \sigma_A$). Thus, as smaller cations are substituted on the A-site (for example, lanthanides of higher atomic number), the ability of a stannate pyrochlores to transform to the disordered phase is enhanced and the material becomes more resistant to electronic excitation-induced amorphization. This mixed in-track phase morphology indicates a radiation response intermediate to those of the titanate and zirconate pyrochlores.

This is consistent with a radiation response governed primarily by the cation ionic radius, as the ionic radius of Sn is between those of Ti and Zr, while the lanthanide elements contract across the lanthanide series. Trivalent Y has an ionic radius between those of Gd and Er, consistent with the phase behavior observed here. The mixed amorphization and disordering of ion-solid interaction regions of the stannate pyrochlores is inconsistent with a radiation response governed primarily by bond covalency, as has been proposed previously[27–30]. These results mirror those of low-energy irradiations by Lumpkin *et al.*[53], who observed an improvement in the radiation tolerance of pyrochlores when Ti was substituted by Sn on the *B*-site.

Ab initio calculations by Jiang *et al.*[54] predicted a lower propensity to disorder for the stannate pyrochlores than for titanate pyrochlores with the same *A*-site cation, suggesting that the former would therefore also exhibit inferior resistance to amorphization under extreme conditions. This finding, which disagrees with the experimental results presented here, was attributed to the influence of the Sn-O bond covalency on the disordering energetics. These calculations assumed a quasi-random distribution of cations and anions on their respective sublattices in a defect-fluorite structure when simulating the disordered phase. However, Shamblin *et al.*[55] have more recently reported that disordered pyrochlores instead adopt a local weberite-type structure[38], wherein half the A- and B-site cations retain the eightfold and sixfold coordination, respectively, that they exhibit in the initial pyrochlore phase. Modulation of these orthorhombic structural units yields the long-range defect-fluorite ordering evident in XRD measurements. Thus, the inconsistency of the experimental observations reported here with previous computational study of pyrochlore disordering may arise from the use of an incorrect structure model in the calculations. The assumption of defect-fluorite local order in the disordered phase requires changes of both the *A*- and *B*-site cation coordination to sevenfold, on

average, significantly affecting the predicted energetics due to the polar covalent nature of the Sn-O bond.

C. Raman spectroscopy: local structure

Raman spectroscopy provides information about the coordination and local ordering of ionic-covalent compounds. It is an ideal probe for the structural characterization of disordered and amorphous materials because it does not require structural periodicity. In contrast, XRD measurements probe long-range structure, which is absent in the irradiation-induced amorphous phase and differs substantially from the short-range structure in the disordered phase[55]. Fig. 6 shows representative Raman spectra of $Nd_2Sn_2O_7$ and $Yb_2Sn_2O_7$ as a function of ion fluence. These are, among the materials studied, the compounds found to be least and most resistant to irradiation-induced amorphization, respectively. The initial spectra of these compounds, as well as all others studied, correspond well to the pyrochlore phase, which exhibits six Raman-active modes[56,57]. The three strongest bands are the overlapping T_{2g} and E_g modes at ~300 cm^{-1}, arising from O-*A*-O bending [58], the T_{2g} mode at ~410 cm^{-1}, and the A_{1g} mode at ~500 cm^{-1}, involving the vibration of O in the 48*f* site[46]. There are also two additional, weaker T_{2g} modes. Stretching of the short *B*-O bonds, which have the strongest force constant in pyrochlore materials[46], does not contribute substantially to any of the Raman-active modes, such that minimal signal is found in the high wavenumber region[59].

With increasing ion fluence, transformations to the disordered and amorphous phases are indicated by the gradual attenuation of all modes corresponding to the pyrochlore structure and the simultaneous growth of new, broad vibrational features. Reduction in the intensity of the pyrochlore modes is analogous to that observed in the XRD maxima, providing further evidence of the loss of pyrochlore-type ordering in all compounds in response to dense electronic

excitation. The bands that grow with increasing ion fluence are attributed to the disordered and amorphous phases that form within ion tracks. A continuum of broad peaks is typical of materials in which translational symmetry has been suppressed, as this yields a relaxation of the selection rules such that phonons from throughout the Brillouin zone contribute to the Raman signal[58].

Surprisingly, the spectra of these materials at the highest ion fluence achieved, 3×10^{13} ions cm^{-2}, are very similar despite large differences in their amorphous and disordered phase fractions (see Figs. 4 and 5). Both compounds show bands centered at ~ 155, 330, and 650 cm^{-1}, differing only in the presence of an additional band at ~450 cm^{-1} in the spectrum of $Yb_2Sn_2O_7$, which is absent in that of $Nd_2Sn_2O_7$. Fig. 7 shows representative spectra from stannate pyrochlores irradiated to this ion fluence, illustrating the generality of these features. This indicates that the disordered and amorphous phases share similar local structure and coordination, despite their differing long-range structures. The peak positions and intensities observed here agree qualitatively with the results of previous Raman spectroscopy measurements of irradiated titanate pyrochlores[15,16,59] and of those amorphized by the application of pressure[60]. This is consistent with the observation of Shamblin *et al.*[55] that the local ordering of disordered pyrochlores is independent of the disordering mechanism.

Comparison of the spectra from all compounds at high ion fluence, whereat the irradiation-induced transformations to either the disordered or amorphous phases are complete, shows that the spectra differ qualitatively only in the intensity of the band at ~450 cm^{-1}, which grows with decreasing *A*-site cation ionic radius and r_A/r_B. The position of this peak matches that of the triply-degenerate T_{2g} mode exhibited by compounds with the fluorite structure[61], suggesting that it arises from medium- and long-range defect-fluorite-like ordering. This

interpretation is consistent with the growth of this peak with increasing tendency of the disordered defect-fluorite phase to form within ion tracks, rather than the amorphous phase (see Fig. 5). However, the spectra of all materials, including those that consist primarily of the disordered phase, differ substantially from the single-mode spectra expected for a material with fluorite-like local ordering. Thus, the short-range structure of the disordered phase does not fully reflect its long-range defect fluorite structure, as indicated by XRD measurements.

Shamblin *et al*. have shown that the local structure of disordered pyrochlore materials consists of orthorhombic weberite-type structural units which are modulated in an aperiodic manner, yielding an average, long-range defect-fluorite structure with cubic symmetry. Raman spectroscopy[62] and selected-area electron diffractions (SAED)[63] measurement of A_3BO_7 compounds with an average, long-range defect fluorite structure also showed evidence of local domains with symmetry distinct from that of the fluorite structure. The weberite-type structure is characterized by chains of corner-sharing BO_6 octahedra and parallel chains of AO_8 distorted cubic polyhedra, which lie in layers parallel to (100) and alternate with layers of sevenfold-coordinated cations[38,64]. In this way, the coordination of *A*- and *B*-site cations is partly retained in the transformation from the pyrochlore structure to a structure with local weberite-type ordering, consistent with electron energy loss spectroscopy (EELS)[65] and EXAFS[46] measurements indicating retention of octahedral coordination of the B-site cation in disordered pyrochlores.

The Raman spectra of irradiated stannate pyrochlores, both those that undergo a transformation to an amorphous phase and those that transform primarily to the disordered phase, show remarkable agreement with the spectra of ternary A_3BO_7 compounds with the weberite-type structure. Weberite-type materials have 27 Raman-active modes: numerous overlapping modes at low wavenumbers (below ~450 cm^{-1}), producing a broad band centered around 350 cm^{-1}, and

a single strong band at higher wavenumbers arising from a BO_6 breathing mode[62,66,67]. Analogous low wavenumber modes, forming a band centered at ~350 cm^{-1}, are exhibited by the irradiated stannate pyrochlores in Fig. 7, along with a single intense band at higher wavenumbers. The latter mode has been previously observed in disordered titanate pyrochlores and was attributed to *B*-O stretching[59], in agreement with its origin in weberite-type local ordering. Its high frequency indicates a relatively short *B*-O bond distance, as is characteristic of the BO_6 polyhedra that are retained in a weberite-type local structure, rather than the sevenfold coordination expected for a short-range defect-fluorite structure. These results confirm, by vibrational spectroscopy, the presence of weberite-type short-range structure in the disordered phase of pyrochlore compounds, despite a long-range defect-fluorite structure of cubic symmetry.

This evidence of weberite-type local ordering in disordered pyrochlore agrees with previous neutron total scattering results[55]. However, the present spectroscopic results further indicate similar weberite-type ordering in amorphous $A_2Sn_2O_7$ compounds. The spectra of amorphous materials match well to those of primarily disordered materials, differing only in the intensity of the single mode at ~450 cm^{-1}, that is related to the presence of partial fluorite-like ordering. Atomistic simulations have predicted local ordering to occur during the amorphization of pyrochlores with high r_A/r_B, such that the sixfold coordination of the *B*-site cation is retained[34]. EELS measurements have also indicated similarity in the short-range structures of disordered and amorphous titanate pyrochlore compounds, based on the observation of similar crystal field splitting of the Ti L-edge in both phases[65].

As the r_A/r_B of the stannate pyrochlore system is reduced through *A*-site cation substitution, two changes to the Raman spectra of the highly irradiated compounds occur. The

Sn-O stretching mode (~650 cm^{-1}) shifts to higher wavenumbers, an effect consistent with calculations showing a monotonic increase in the Sn-O force constant with decreasing r_A[57] and also observed in A_3BO_7 weberite-structured compounds[62]. Additionally, the mode at ~450 cm^{-1} shifts and increases in intensity as the cation ionic radii become more similar and the disordered phase fraction increases. This mode is attributed to the contribution of the fluorite-like component of ordering, explaining its near absence in the spectra of the fully amorphous materials $Nd_2Sn_2O_7$ and $Sm_2Sn_2O_7$, and its gradual growth with σ_D (see Fig. 5). With the intensity of this mode corresponding to the degree of fluorite-like ordering accompanying the modulation of the local weberite-type units, it is clear that this fluorite-like character is inversely proportional to r_A/r_B. Thus, when electronic excitation induces a transformation of pyrochlore compounds to phases with weberite-type local structures, the cation ionic radius mismatch determines the extent to which modulation of these weberite units yields long-range crystallinity in an average defect-fluorite structure, rather than a fully aperiodic arrangement of these structural units in an amorphous phase.

IV. CONCLUSIONS

The structural transformations of stannate pyrochlores induced by dense electronic excitation are complex, multiscale, and highly composition-dependent. Upon relaxation of the transient, high-energy state produced by swift heavy ion irradiation, these compounds can adopt either amorphous or disordered phases, with many materials in this system exhibiting a mixture of both phases within individual ion tracks. Amorphization is favored in compounds with large r_A/r_B, whereas disordering is favored in those with small r_A/r_B. The local structures of both phases are similar, exhibiting weberite-type short-range ordering. They differ in that long-range

order is absent in the amorphous phase, while modulation of the weberite-type ordering yields an average, long-range defect-fluorite structure in the disordered phase. The increasing resistance of stannate pyrochlores to irradiation-induced amorphization with decreasing r_A/r_B represents increasing favorability of the modulation of weberite units into this long-range average structure.

Because both pyrochlore-to-amorphous and amorphous-to-disordered processes occur in individual ion tracks, phase modification of these materials by swift heavy ion irradiation is best described by a model that accounts for both amorphization of crystalline material near the energetic interior of a cylindrical ion-solid interaction region and epitaxial recrystallization of amorphous material near amorphous/crystalline interfaces. Rapid quenching in track cores precludes the complete recovery of fluorite-like long-range ordering. Slower quenching and the presence of a crystalline "template" interface with fluorite-derivative ordering near track peripheries enable the arrangement of weberite-type structural units into a modulated, average defect-fluorite structure in materials with relatively small r_A/r_B.

This competition between amorphization and disordering contrasts with the behavior of titanate pyrochlores, which have smaller *B*-site cations and tend to amorphize, and zirconate pyrochlores, which have larger *B*-site cations and tend to disorder. Thus, the behavior of the stannate system is consistent with a radiation response governed largely by the cation ionic radii. It is inconsistent with a substantial effect of bond covalency, since the Sn-O bond is more covalent than the Ti-O bond, yet the stannate pyrochlores are consistently more resistant to amorphization than titanate pyrochlores with the same *A*-site cation. While the *B*-O bond covalency may influence the radiation response of pyrochlore materials, the magnitude of this effect appears to be small compared with the effect of the cation ionic radius mismatch.

ACKNOWLEDGEMENTS

This work was supported by the Energy Frontier Research Center *Materials Science of Actinides* funded by the U.S. Department of Energy (DOE), Office of Science, Office of Basic Energy Sciences (Grant No. DE-SC0001089). This work is based upon research conducted at the Cornell High Energy Synchrotron Source (CHESS) which is supported by the National Science Foundation and the National Institutes of Health/National Institute of General Medical Sciences under NSF award DMR-1332208. J.S. acknowledges support from Organized Research Unit funding through the University of Tennessee Office of Research.

REFERENCES

[1] J.S. Gardner, M.J.P. Gingras, and J.E. Greedan, Rev. Mod. Phys. **82**, 53 (2010).

[2] C.R. Wiebe and A.M. Hallas, APL Mater. **3**, 041519 (2015).

[3] R.C. Ewing, W.J. Weber, and J. Lian, J. Appl. Phys. **95**, 5949 (2004).

[4] J. Wu, X. Wei, N.P. Padture, P.G. Klemens, M. Gell, E. García, P. Miranzo, and M.I. Osendi, J. Am. Ceram. Soc. **85**, 3031 (2002).

[5] P.K. Schelling, S.R. Phillpot, and R.W. Grimes, Philos. Mag. Lett. **84**, 127 (2004).

[6] B. Wuensch, K.W. Eberman, C. Heremans, E.M. Ku, P. Onnerud, E.M.E. Yeo, S.M. Haile, J.K. Stalick, and J.D. Jorgensen, Solid State Ionics **129**, 111 (2000).

[7] M. Subramanian, G. Aravamudan, and G.V. Subba Rao, Prog. Solid State Chem. **15**, 55 (1983).

[8] S. Park, M. Lang, C.L. Tracy, J. Zhang, F. Zhang, C. Trautmann, M.D. Rodriguez, P. Kluth, and R.C. Ewing, Acta Mater. **93**, 1 (2015).

[9] G.J. Redhammer, G. Roth, and G. Amthauer, Acta Crystallogr. C **63**, 93 (2007).

[10] D. Michel, M. Perez y Jorba, and R. Collongues, Mat. Res. Bull. **9**, 1457 (1974).

[11] F.X. Zhang, M. Lang, Z. Liu, and R.C. Ewing, Phys. Rev. Lett. **105**, 015503 (2010).

[12] F. Zhang, M. Lang, C. Tracy, R.C. Ewing, D.J. Gregg, and G.R. Lumpkin, J. Solid State Chem. **219**, 49 (2014).

[13] J. Zhang, M. Lang, R.C. Ewing, R. Devanathan, W.J. Weber, and M. Toulemonde, J. Mater. Res. **25**, 1344 (2010).

[14] M.K. Patel, V. Vijayakumar, S. Kailas, D.K. Avasthi, J.C. Pivin, and A.K. Tyagi, J. Nucl. Mater. **380**, 93 (2008).

[15] M. Lang, F.X Zhang, R.C. Ewing, J. Lian, C. Trautmann, and Z. Wang, J. Mater. Res. **24**, 1322 (2009).

[16] M. Lang, J. Lian, J. Zhang, F. Zhang, W.J. Weber, C. Trautmann, and R.C. Ewing, Phys. Rev. B **79**, 224105 (2009).

[17] G. Sattonnay, S. Moll, L. Thomé, C. Legros, A. Calvo, M. Herbst-Ghysel, C. Decorse, and I. Monnet, Nucl. Instrum. Meth. B **272**, 261 (2012).

[18] G. Sattonnay, C. Grygiel, I. Monnet, C. Legros, M. Herbst-Ghysel, and L. Thomé, Acta Mater. **60**, 22 (2012).

[19] N. Itoh, D.M. Duffy, S. Khakshouri, and A.M. Stoneham, J. Phys.: Condens. Matter **21**, 474205 (2009).

[20] A.V. Lankin, I.V. Morozov, G.E. Norman, S.A. Pikuz, and I.Y. Skobelev, Phys. Rev. E **79**, 036407 (2009).

[21] D.M. Duffy, S.L. Daraszewicz, and J. Mulroue, Nucl. Instrum. Meth. B **277**, 21 (2012).

[22] M. Lang, M. Toulemonde, J. Zhang, F. Zhang, C.L. Tracy, J. Lian, Z. Wang, W.J. Weber, D. Severin, M. Bender, C. Trautmann, and R.C. Ewing, Nucl. Instrum. Meth. B **336**, 102 (2014).

[23] M. Lang, F. Zhang, J. Zhang, J. Wang, J. Lian, W.J. Weber, B. Schuster, C. Trautmann, R.

Neumann, and R.C. Ewing, Nucl. Instrum. Meth. B **268**, 2951 (2010).

[24] G. Sattonnay, S. Moll, L. Thomé, C. Decorse, C. Legros, P. Simon, J. Jagielski, I. Jozwik, and I. Monnet, J. Appl. Phys. **108**, 103512 (2010).

[25] K.E. Sickafus, L. Minervini, R.W. Grimes, J.A. Valdez, M. Ishimaru, F. Li, K.J. McClellan, and T. Hartmann, Science **289**, 748 (2000).

[26] M.J.D. Rushton, C.R. Stanek, A.R. Cleave, B.P. Uberuaga, K.E. Sickafus, and R.W. Grimes, Nucl. Instrum. Meth. B **255**, 151 (2007).

[27] H.M. Naguib and R. Kelly, Radiat. Eff. **25**, 1 (1975).

[28] K. Trachenko, J.M. Pruneda, E. Artacho, and M.T. Dove, Phys. Rev. B **71**, 184104 (2005).

[29] K. Trachenko, J. Phys.: Condens. Matter **16**, 1491 (2004).

[30] K. Trachenko, M. Pruneda, E. Artacho, and M.T. Dove, Phys. Rev. B **70**, 134112 (2004).

[31] J. Shamblin, C.L. Tracy, R.C. Ewing, F. Zhang, W. Li, C. Trautmann, and M. Lang, doi: 10.1016/j.actamat.2016.07.017 (to be published)

[32] R.D. Shannon, Acta Cryst. **32**, 751 (1976).

[33] J.M. Pruneda and E. Artacho, Phys. Rev. B **72**, 085107 (2005).

[34] G. Sattonnay and R. Tétot, J. Phys.: Condens. Matter **26**, 055403 (2014).

[35] W.R. Panero, L.P. Stixrude, and R.C. Ewing, Phys. Rev. B **70**, 054110 (2004).

[36] G.R. Lumpkin, M. Pruneda, S. Rios, K.L. Smith, K. Trachenko, K.R. Whittle, and N.J. Zaluzec, J. Solid State Chem. **180**, 1512 (2007).

[37] T. Ikeda, M. Sakata, M. Takata, B.J. Kennedy, D.J. Cookson, C.J. Howard, Jpn. J. Appl. Phys. **38**, 93 (1999).

[38] L. Cai and J.C. Nino, Acta Cryst. B **65**, 269 (2009).

[39] M. Lang, C.L. Tracy, R.I. Palomares, F. Zhang, D. Severin, M. Bender, C. Trautmann, C.

Park, V.B. Prakapenka, V.A. Skuratov, and R.C. Ewing, J. Mater. Res. **30**, 1366 (2015).

[40] J.F. Ziegler, M.D. Ziegler, and J.P. Biersack, Nucl. Instrum. Meth. B **268**, 1818 (2010).

[41] A.P. Hammersley, S.O. Svensson, M. Hanfland, A.N. Fitch, and D. Häusermann, High Press. Res. **14**, 235 (1996).

[42] G.K. Williamson and W.H. Hall, Acta Metall. **1**, 22 (1953).

[43] B.E. Warren, J. Am. Ceram. Soc. **17**, 249 (1934).

[44] J. Lian, X.T. Zu, K.V.G. Kutty, J. Chen, L.M. Wang, and R.C. Ewing, Phys. Rev. B **66**, 054108 (2002).

[45] J. Lian, K.B. Helean, B.J. Kennedy, L.M. Wang, A. Navrotsky, and R.C. Ewing, J. Phys. Chem. B **110**, 2343 (2006).

[46] N.J. Hess, B.D. Begg, S.D. Conradson, D.E. McCready, P.L. Gassman, and W.J. Weber, J. Phys. Chem. B **106**, 4663 (2002).

[47] X. Qiu-rong, Z. Jian, Y. Dong-min, G. Qi-Xun, and L. Ning, Chinese Phys. B **24**, 126103 (2015).

[48] J.F. Gibbons, Proc. IEEE **60**, 1062 (1972).

[49] S. Moll, G. Sattonnay, L. Thomé, J. Jagielski, C. Decorse, P. Simon, I. Monnet, and W.J. Weber, Phys. Rev. B **84**, 064115 (2011).

[50] K. Yasuda, M. Etoh, K. Sawada, T. Yamamoto, K. Yasunaga, S. Matsumura, and N. Ishikawa, Nucl. Instrum. Meth. B **314**, 185 (2013).

[51] F.F. Morehead and B.L. Crowder, Radiat. Eff. **6**, 27 (1970).

[52] W.J. Weber, Nucl. Instrum. Meth. B **166-167**, 98 (2000).

[53] G.R. Lumpkin, K.L. Smith, M.G. Blackford, K.R. Whittle, E.J. Harvey, S.A.T. Redfern, and N.J. Zaluzec, Chem. Mater. **21**, 2746 (2009).

[54] C. Jiang, C.R. Stanek, K.E. Sickafus, and B.P. Uberuaga, Phys. Rev. B **79**, 104203 (2009).

[55] J. Shamblin, M. Feygenson, J. Neuefeind, C.L. Tracy, F. Zhang, S. Finkeldei, D. Bosbach, H. Zhou, R.C. Ewing, and M. Lang, Nat. Mater. **15**, 507 (2016).

[56] M.T. Vandenborre, E. Husson, J.P. Chatry, and D. Michel, J. Raman Spectrosc. **14**, 63 (1983).

[57] H.C. Gupta, S. Brown, N. Rani, and V.B. Gohel, Int. J. Inorg. Mater. **3**, 983 (2001).

[58] D. Michel, M. Perez y Jorba, and R. Collongues, J. Raman Spectrosc. **5**, 163 (1976).

[59] M.L. Sanjuán, C. Guglieri, S. Díaz-Moreno, G. Aquilanti, A.F. Fuentes, L. Olivi, and J. Chaboy, Phys. Rev. B **84**, 104207 (2011).

[60] F. Zhang, B. Manoun, S.K. Saxena, and C.S. Zha, Appl. Phys. Lett. **86**, 181906 (2005).

[61] V.G. Keramidas and W.B. White, J. Chem. Phys. **59**, 1561 (1973).

[62] K.P.F. Siqueira, J.C. Soares, E. Granado, E.M. Bittar, A.M. de Paula, R.L. Moreira, and A. Dias, J. Solid State Chem. **209**, 63 (2014).

[63] L. Lõpez-Conesa, J.M. Rebled, M.H. Chambrier, K. Boulahya, J.M. González-Calbet, M.D. Braida, G. Dezanneau, S. Estradé, and F. Peiró, Fuel Cells **13**, 29 (2013).

[64] H.J. Rossell, J. Solid State Chem. **27**, 115 (1979).

[65] R. Sachan, B. Liu, D. Aidhy, Y. Zhang, M.F. Chisholm, and W.J. Weber, Microsc. Microanal. **21**, 1333 (2015).

[66] N. Preux, A. Rolle, C. Merlin, M. Benamira, M. Malys, C. Estournes, A. Rubbens, and R.N. Vannier, Comptes Rendus Chim. **13**, 1351 (2010).

[67] K.P.F. Siqueira, R.M. Borges, E. Granado, L.M. Malard, A.M. de Paula, R.L. Moreira, E.M. Bittar, and A. Dias, J. Solid State Chem. **203**, 326 (2013).

FIG. 1. TEM image of ion tracks in $Nd_2Sn_2O_7$ irradiated with 2.2 GeV Au ions to a fluence of 1×10^{11} ions cm^{-2}. The linear, parallel areas of dark contrast indicate cylindrical volumes through which an ion has passed and modified the material's structure. Similar continuous, linear, oriented tracks were observed in all materials studied.

FIG. 2. The energy per unit path length deposited by 2.2 GeV Au ions to the electronic subsystem of each material studied, as calculated using the SRIM code[40]. The legend is sorted by *A*-site cation ionic radius, and thus also by the material's r_A/r_B. Within the sample thickness, the electronic energy loss increases as heavier cations of smaller ionic radius are substituted on the *A*-site, with the exception of $Y_2Sn_2O_7$. While Y is chemically similar to the lanthanide elements, it is much lighter, resulting in a relatively low density of this compound and its low energy transfer per unit path length. All data are corrected for the densities of the wafer samples.

FIG. 3. Representative XRD patterns from several stannate pyrochlores irradiated with 2.2 GeV Au ions to various ion fluences. The materials are sorted from high (left) to low (right) *A*-site cation ionic radius, and thus r_A/r_B. The initial patterns of all materials correspond to a pyrochlore structure, which is lost as irradiation proceeds. Materials with large *A*-site cations exhibit the growth of broad scattering features typical of amorphous phases. Those with small *A*-site cations show minimal amorphization, preferential attenuation of peaks related to pyrochlore superstructure ordering, and retention of peaks related to fluorite substructure ordering. This indicates a transformation from the pyrochlore phase to a phase with a long-range defect-fluorite structure.

FIG. 4. Amorphous phase fractions of three stannate pyrochlores as a function of ion fluence. As the ionic radius of the *A*-site cation decreases, so too does the amorphous fraction at a given ion fluence. This indicates inverse proportionality between r_A/r_B and the propensity of these materials to disorder, rather than amorphize. The dashed lines show a fit of Eq. (5) to the data. Error bars represent the standard error of amorphous fractions determined from deconvolution of multiple XRD patterns.

FIG. 5. Ion track cross-sectional areas for the two transformations observed in XRD measurements, amorphization and disordering (σ_A and σ_D). While the net track area stays relatively constant as a function of composition and r_A/r_B, the proportion of each phase within individual tracks varies dramatically. As r_A/r_B decreases, the volume of amorphous material within an individual ion track decreases, while the volume of disordered material increases. The small deviation from the regular variation in σ_A and σ_D as a function of r_A/r_B, apparent at r_A/r_B = 1.477, is due to the relatively low density of $Y_2Sn_2O_7$ and its effect on ion energy deposition. Error bars represent the uncertainty in the fitting of Eq. (5) to phase fraction data. The solid lines are a guide for the eye.

FIG. 6. Representative Raman spectra of $Nd_2Sn_2O_7$ and $Yb_2Sn_2O_7$ as a function of 2.2 GeV Au ion fluence. These materials have the largest and smallest *A*-site cations, respectively, among the materials studied. The initial spectra of both compounds match well to the predicted Raman-active modes of the pyrochlore phase. Upon irradiation, the spectra of both materials exhibit gradual attenuation of the initial vibrational modes and the growth of new, broad bands. The final spectra of both materials ($\Phi = 3\times10^{13}$ ions cm^{-2}, at which they are fully transformed) are

qualitatively similar, differing only in the presence of an additional peak at ~450 cm^{-1} in the spectrum of $Yb_2Sn_2O_7$.

FIG. 7. Raman spectra of several stannate pyrochlores following irradiation to a fluence of 3×10^{13} ions cm^{-2}. The spectra are stacked in order of *A*-site cation ionic radius (decreasing from bottom to top). All spectra are qualitatively similar, illustrating the commonality of the weberite-type local structure to the disordered and amorphous phases. As smaller cations are substituted on the *A*-site, a peak at ~450 cm^{-1} (marked by the grey arrows) grows in intensity. This peak is attributed to the fluorite-like ordering present in irradiated pyrochlores with small r_A/r_B. This peak and that at ~650 cm^{-1}, which is attributed to Sn-O stretching, shift to higher wavenumbers as the *A*-site cation ionic radius decreases.

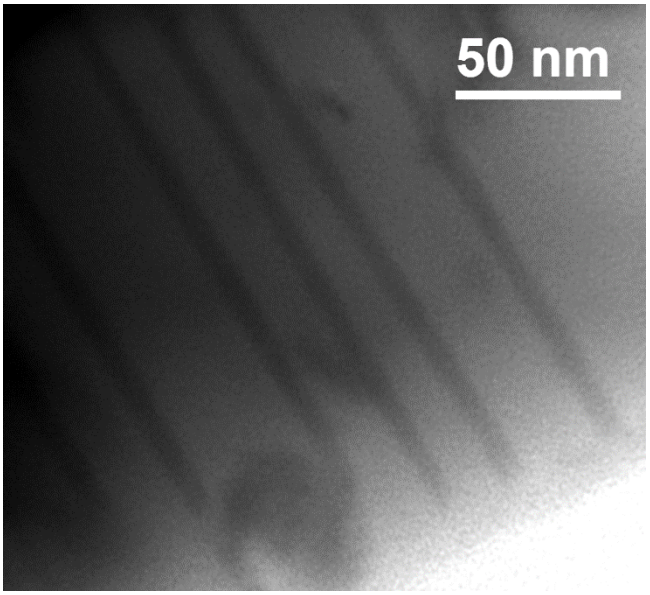

FIG. 1

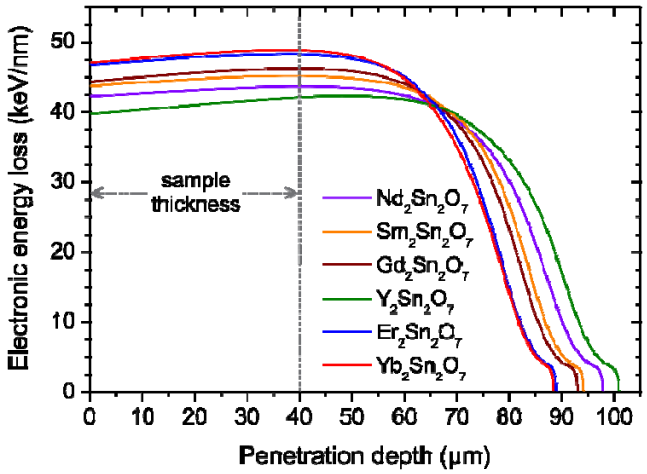
Electronic energy loss (keV/nm)
Penetration depth (μm)
sample thickness
Nd2Sn2O7
Sm2Sn2O7
Gd2Sn2O7
Y2Sn2O7
Er2Sn2O7
Yb2Sn2O7
0
10
20
30
40
50
60
70
80
90
100

FIG. 2

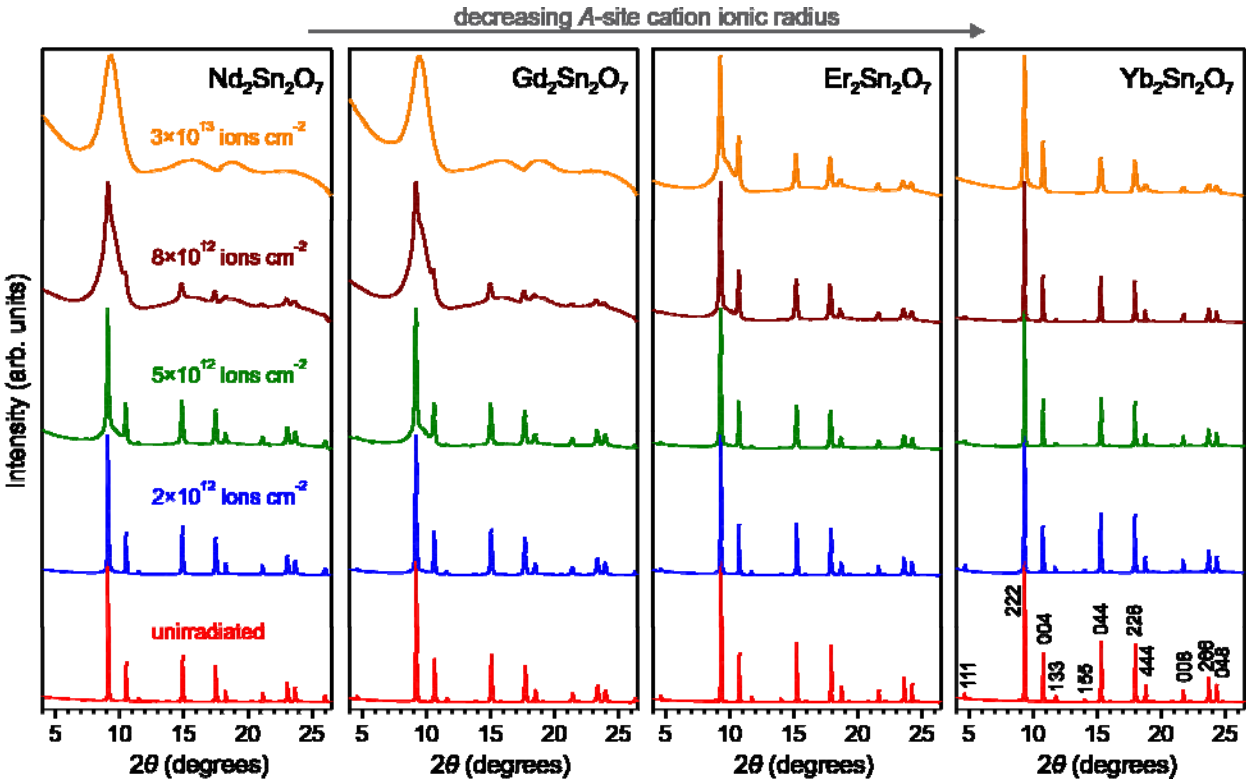
decreasing A-site cation ionic radius
Nd2Sn2O7
Gd2Sn2O7
Er2Sn2O7
Yb2Sn2O7
3×10^13 ions cm^-2
8×10^12 ions cm^-2
5×10^12 ions cm^-2
2×10^12 ions cm^-2
unirradiated
Intensity (arb. units)
2θ (degrees)
111
222
004
133
155
044
228
444
008
288
048

FIG. 3

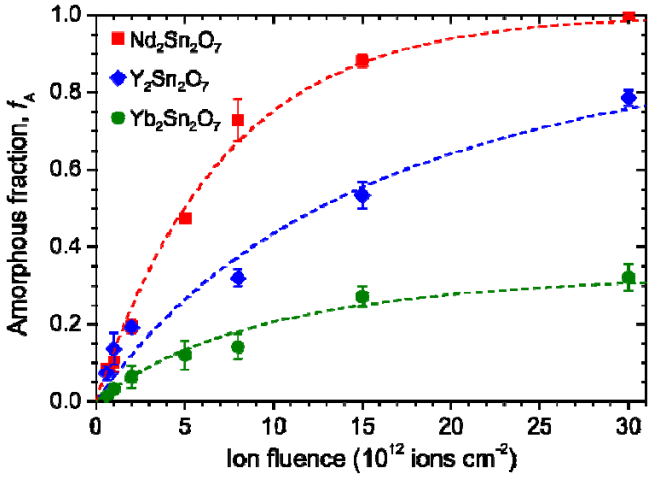
Nd2Sn2O7
Y2Sn2O7
Yb2Sn2O7
Amorphous fraction, fA
Ion fluence (10^12 ions cm^-2)
0.0
0.2
0.4
0.6
0.8
1.0
0
5
10
15
20
25
30

FIG. 4

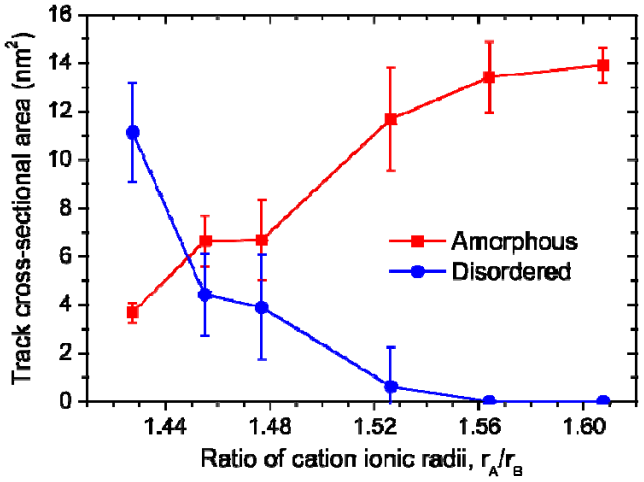
Track cross-sectional area (nm²)
Ratio of cation ionic radii, r_A/r_B
Amorphous
Disordered
0
2
4
6
8
10
12
14
16
1.44
1.48
1.52
1.56
1.60

FIG. 5

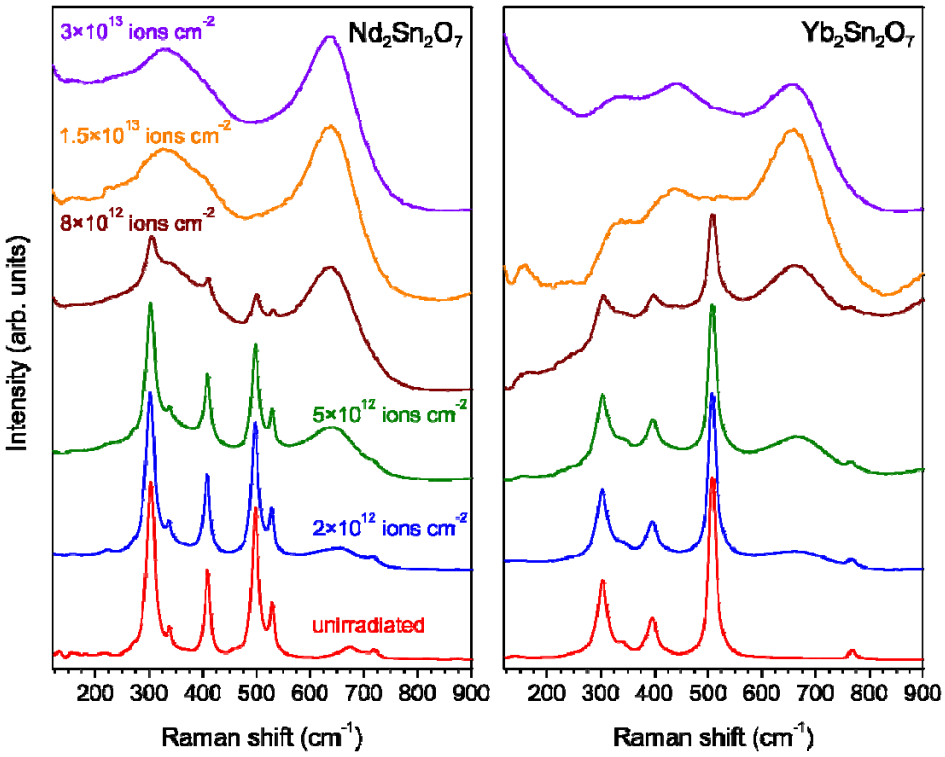
3×10^13 ions cm^-2
1.5×10^13 ions cm^-2
8×10^12 ions cm^-2
5×10^12 ions cm^-2
2×10^12 ions cm^-2
unirradiated
Nd2Sn2O7
Yb2Sn2O7
Intensity (arb. units)
200 300 400 500 600 700 800 900
Raman shift (cm^-1)

FIG. 6

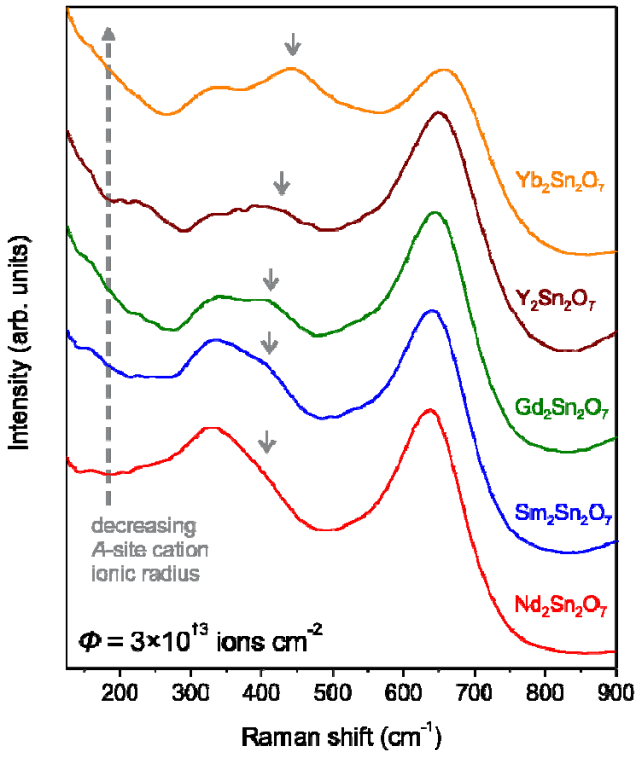
Intensity (arb. units)
Raman shift (cm^{-1})
200
300
400
500
600
700
800
900
$Yb_2Sn_2O_7$
$Y_2Sn_2O_7$
$Gd_2Sn_2O_7$
$Sm_2Sn_2O_7$
$Nd_2Sn_2O_7$
decreasing
A-site cation
ionic radius
$\Phi = 3\times10^{13}$ ions cm^{-2}

FIG. 7